Controlled growth of a graphdiyne/cobalt hydroxide heterointerface for efficient chlorine production

LIU Hui-min[1], LUAN Xiao-yu[1], YAN Jia-yu[1], BU Fan-le[1], XUE Yu-rui[1,*], LI Yu-liang[1,2,*]

（1. *Shandong Provincial Key Laboratory for Science of Material Creation and Energy Conversion, Science Center for Material Creation and Energy Conversion, School of Chemistry and Chemical Engineering, Shandong University, Jinan* 250100, *China*;
2. *Institute of Chemistry, Chinese Academy of Sciences, Beijing* 100190, *China*）

Abstract: The chlor-alkali process plays a key and irreplaceable role in the chemical industry because of its use in various industrial processes. However, the low selectivity and efficiency of the reported chlorine evolution reaction (CER) electrocatalysts obviously hinder its practical use. We report a simple method for the controlled growth of high-performance CER electrocatalysts by first growing cobalt hydroxide on the surface of carbon cloth, followed by the in-situ growth of graphdiyne (GDY/$Co(OH)_2$). As expected, the as-synthesized catalyst has a small overpotential of only 83 mV at 10 mA cm^{-2}, a maximum Faradaic Efficiency (FE) of 91.54%, and a high chlorine yield of 157.11 mg h^{-1} cm^{-2} in acidic simulated seawater. Experimental results demonstrate that the in-situ growth of GDY on the $Co(OH)_2$ surface leads to the formation of heterointerfaces with strong electron transfer between GDY and Co atoms, resulting in a higher conductivity, larger active specific surface area and more active sites, thereby improving the overall electrocatalytic selectivity and efficiency.

Key words: Carbon material; Graphdiyne; High selectivity; Heterointerface; Chlorine evolution reaction

1 Introduction

Chlorine plays a crucial role in modern chemical industries including water treatment, disinfection, advanced technology and the products that contribute to public health and safety[1–4]. During the past decades, dimensionally stable anodes (DSAs) based on RuO_2 and IrO_2 have been established as electrocatalysts for chlor-alkali process, but limited by their intrinsic poor activity and low selectivity[5,6]. Besides, the RuO_2 and IrO_2 species in DSA are supposed to be active for oxygen evolution reaction (OER), which is the key competitive reaction to chlorine evolution reaction (CER)[7], unavoidably reducing the overall electrocatalytic performances regarding the CER[8–11]. The design and synthesis of Ru/Ir-free catalysts with high selectivity and efficiency towards chlorine production from seawater are still in great demand.

Graphdiyne (GDY) has attracted increasing attention in various catalysis and energy-related applications because of its unique structures and properties such as the alkyne-rich structures, high intrinsic activity, the abundance of sp-hybridized pores, high conductivity, and strong integer charge transfer between GDY and metal atoms[12–19]. Especially, the property of GDY that it can be grown on the surface of any substrate provides significant advantages for the controlled growth of heterointerface structures with excellent selectivity, activity and stability[20–23]. Extensive studies have demonstrated that GDY is an ideal platform for constructing new materials with excellent selectivity, activity and stability[24–27]. Various GDY-based materials were successfully synthesized and used as highly efficient electrocatalysts for various chemical conversion reactions including the oxygen evolution reactions[21,28], hydrogen evolution reactions[29–32], N_2/CO_2/O_2 reduction reactions[33–38] and methanol oxidation reactions[39–41]. However, the design of GDY-based electrocatalysts for CER has not been reported. Transition metal-based materials are

Received date: 2024-04-17; **Revised date:** 2024-05-01

Corresponding author: XUE Yu-rui, Professor. E-mail: yrxue@sdu.edu.cn;
LI Yu-liang, Professor. E-mail: ylli@iccas.ac.cn

Author introduction: LIU Hui-min, Master student. E-mail: 2116178973@qq.com

Supplementary data associated with this article can be found in the online version.

considered efficient catalysts to replace noble metals due to their affordability and convenient industrial production processes[42–49]. On another hand, recent studies show that cobalt atoms possess stronger Cl^- binding energy for pre-adsorption of Cl^-, which might benefit the following activation of Cl^- to Cl_2[50,51].

Herein, the graphdiyne/cobalt hydroxide (GDY/$Co(OH)_2$) heterostructured catalysts with high-performance heterointerfaces were synthesized through a facile method to in-situ grow the GDY on the surface of $Co(OH)_2$ nanowires. Experimental results demonstrate that the in-situ growth of GDY on the $Co(OH)_2$ surface leads to the formation of heterointerfaces with strong electron transfer between GDY and Co atoms, resulting in higher conductivity, larger active specific surface area and more active sites, thereby improving the overall electrocatalytic selectivity and efficiency. The as-synthesized GDY/$Co(OH)_2$ was successfully used as the catalyst for CER, achieving the high FE of 91.54%, chlorine yield rates (Y_{AC}) of 157.11 mg h^{-1} cm^{-2}, low overpotential of 83 mV at 10 mA cm^{-2}, as well as good long-term stability for continuous CER at room temperature and ambient pressure in the acidic 0.5 mol L^{-1} NaCl solution.

2 Experimental

2.1 Materials

Cobalt nitrate hexahydrate ($Co(NO_3)_2·6H_2O$) and urea ($CO(NH_2)_2$) were provided by Energy Chemical. Ammonium fluoride (NH_4F), pyridine, N,N-dimethylformamide (DMF), and acetone were purchased from Shanghai Sinopharm Chemical Reagent Co. Ltd., China. Carbon cloth was cleaned before use. The ultrapure water was obtained from a Millipore system. All the reagents were of analytical grade and were used without further purification.

2.2 Synthesis of $Co(OH)_2$

Cobalt hydroxide ($Co(OH)_2$) was synthesized through a hydrothermal method. Briefly, 2 mmol of $Co(NO_3)_2·6H_2O$, 4 mmol of NH_4F, and 7.5 mmol of $CO(NH_2)_2$ were firstly dissolved in 40 mL of deionized water under ultrasonication. The obtained homogeneous solution was then transferred into a 50 mL PTFE-lined autoclave containing a piece of freshly-treated carbon cloth (2 cm×3 cm). The autoclave was placed in an oven at 120 °C for 12 h. After cooling to room temperature, the obtained samples were washed thoroughly by deionized water and dried at room temperatures.

2.3 Synthesis of GDY/$Co(OH)_2$

A piece of $Co(OH)_2$ (2 cm×3 cm) was immersed into a three-necked flask containing 30 mL of pyridine. The pyridine solution of HEB (0.3 mg mL^{-1}, 50 mL) was slowly dropwise added into the above reactor under the protection of argon at 120 °C for 12 h. The obtained GDY/$Co(OH)_2$ was washed thoroughly by hot DMF and acetone.

2.4 Characterizations

Scanning electron microscopy (SEM, Zeiss Gemini 300), transmission electron microscopy (TEM, JEOL-1011) and high-resolution transmission electron microscopy (HRTEM, Talos) images were conducted to obtain the morphologies of the catalysts. Raman spectra were obtained using a Renishaw-2000 Raman spectrometer with a 473 nm excitation laser source. X-ray photoelectron spectroscopy (XPS) measurements were conducted using a Thermo Scientific Escalab 250Xi instrument with 200 W monochromated Al *K*a radiation to analyze the chemical composition and elemental states.

2.5 Electrochemical tests

All electrochemical measurements were conducted using an electrochemical workstation (CHI 660E, China) in an H-type cell (separated by Nafion 117 membrane) with the freshly-prepared catalysts, graphite rod and saturated calomel electrode as the working electrode, counter electrode and reference electrode, respectively. The mass loading of freshly-prepared GDY/$Co(OH)_2$ is 2.7 mg cm^{-2}. The electrolyte was a mixture containing 0.5 mol L^{-1} NaCl and 0.1 mol L^{-1} HCl (saturated with argon before use). Linear sweep voltammetry (LSV) measurements were conducted at a scan rate of 5 mV s^{-1}. The long-term stability tests of the catalysts were performed using the chronoamperometric method under a constant overpotential. Electrochemical impedance spectroscopy (EIS)

was performed at open circuit voltage in the frequency range of 100 kHz to 0.01 Hz. All the measured potential was calibrated using the reversible hydrogen electrode (RHE).

2.6 Quantification of active chlorine

The qualitative and quantitative determination of active chlorine was carried out by N,N-diethyl-p-phenylenediamine (DPD) spectrophotometric method. Firstly, 1.0 mL of the test solution was diluted to the detection range and added to the test tube. Then, 1.0 mL of phosphate buffer (pH = 6.5) and 1.0 mL of DPD reagent were added to the above solution. UV-vis spectrophotometer was conducted from 400 to 700 nm to measure the absorption spectra as quickly as possible. The calibration curve was plotted at 552 nm using absorbance versus the concentration of active chlorine. The DPD reagent solution was prepared by dissolving 0.1 g of N,N-Diethyl-p-phenylenediamine sulfate in pure water with 0.2 mL of concentrated H_2SO_4, and then diluting the solution to 100 mL (The solution was stored in a brown bottle and kept in a cold, dark environment. If the color of the solution turns red or fades, it should be reconstituted).

3 Results and discussion

Fig. 1 illustrates the synthesis route of GDY/$Co(OH)_2$ heterostructures through a simple two-step method, including the first synthesis of $Co(OH)_2$ electrode by a hydrothermal method, followed by in-situ growing GDY on the surface of $Co(OH)_2$.

Scanning electron microscopy (SEM) images show that $Co(OH)_2$ nanowires were successfully synthesized and vertically stood on the surface of carbon cloth (Fig. 2a-c), forming a nanowire array morphology that could facilitate the mass transport and provide larger electrochemically active areas. Such morphology was well preserved after in-situ growth of GDY on the $Co(OH)_2$ surface, but with a rougher surface (Fig. 2d-f), which might result in more exposed surface atoms serving as potential catalytic sites, thus improving the overall catalytic performance of the catalyst. The elemental distribution test of GDY/$Co(OH)_2$ (Fig. 2g-i and Fig. S1) reveals the uniform distribution of C, O and Co elements on the catalyst.

The detailed characterizations on the structure of the samples were further conducted using high-resolution transmission electron microscopy (HRTEM). Two typical (101) and (110) crystal planes (with the lattice spacing of 0.237 nm in Fig. 3a and 0.156 nm in Fig. 3b, respectively) of β-$Co(OH)_2$ were observed. The selected area electron diffraction (SAED) pattern

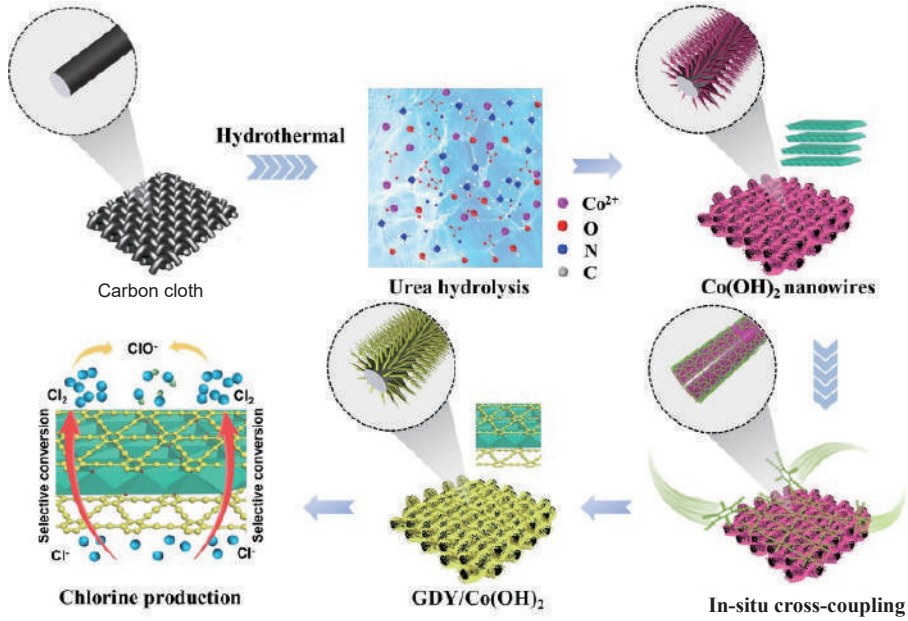

Fig. 1　Schematic illustration of the synthesis route for GDY/$Co(OH)_2$

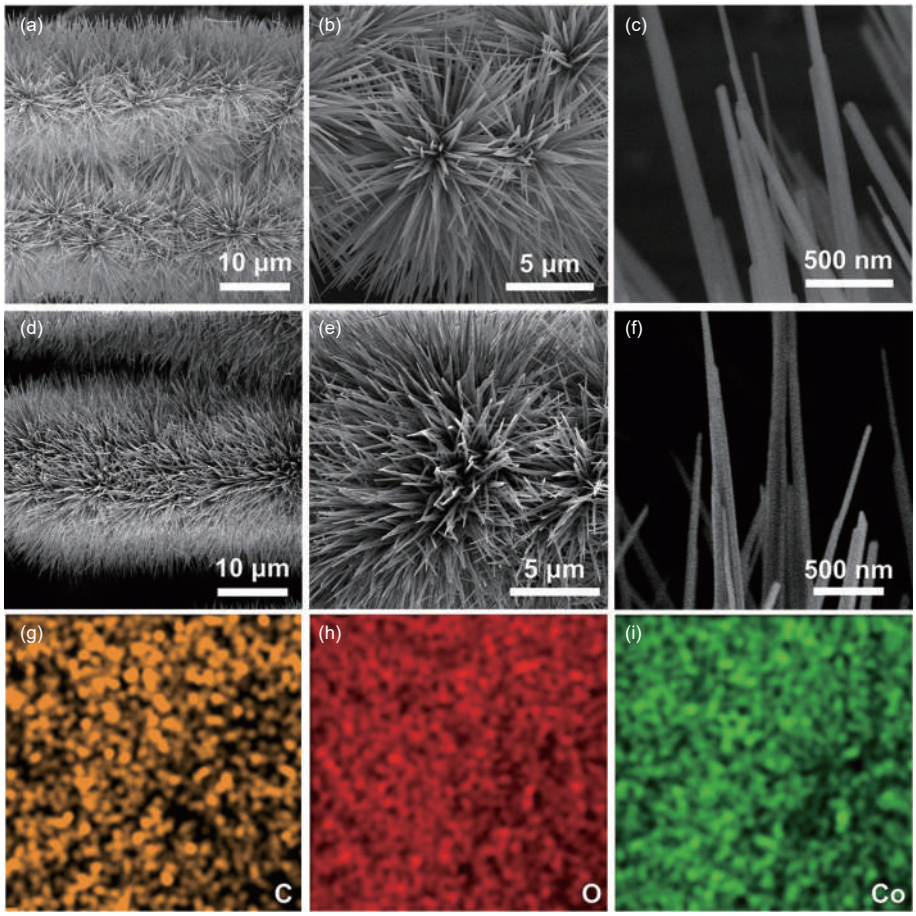

Fig. 2 SEM images of (a-c) $Co(OH)_2$ and (d-f) GDY/$Co(OH)_2$. (g-i) Elemental mapping images of GDY/$Co(OH)_2$

showed diffraction spots for the (101) and (110) crystal planes (Fig. 3c). These results confirm the successful preparation of $Co(OH)_2$ with β phase. Fig. 3d shows that there is an obvious interfacial structure between $Co(OH)_2$ and GDY, which demonstrates the successful formation of GDY/$Co(OH)_2$ heterojunction. GDY presents a layer distance of 0.364 nm (Fig. 3e). The lattice spacings of $Co(OH)_2$ phases changed from 0.156 to 0.150 nm (Fig. 3f), which might be due to the strong interaction between GDY and $Co(OH)_2$ phases. The (100) crystal face of $Co(OH)_2$ with a lattice spacing of 0.280 nm was observed in Fig. 3g and 3h. The elemental distribution mapping (Fig. 3i) showed that the elements Co, O, and C were uniformly distributed in GDY/$Co(OH)_2$.

The Raman spectra of GDY/$Co(OH)_2$ (Fig. 4a) exhibited 4 peaks at 1 366.0, 1 563.2, 1 930.0, and 2 163.0 cm^{-1}, corresponding to the *D*-band, *G*-band, and alkyne bonding vibrational peaks in the structure of GDY, respectively. The presence of alkyne bonding peaks in GDY/$Co(OH)_2$ confirms the successful growth of GDY on the Co(OH) surface. And the shift of the acetylene bond peak position in Raman spectra confirms the interaction between GDY and $Co(OH)_2$. In addition, the I_D/I_G value of pure GDY was 0.69, while that of GDY/$Co(OH)_2$ was 0.76, indicating that more defects were generated after the formation of the heterostructure. This could effectively increase the number of active catalytic sites, facilitate the catalytic reactions, and consequently enhance the overall catalytic performance for chlorine production. The hydrophilicity tests of GDY/$Co(OH)_2$ and pure carbon cloth are presented in Fig. 4b. The experimental results indicated that the surface of pure carbon cloth was hydrophobic. GDY/$Co(OH)_2$ exhibited super hydrophilic properties with a water contact angle of 0°. This improves the wettability of the electrolyte on the surface of the GDY/$Co(OH)_2$ catalyst, facilitating the activation of the reactants at the catalytic interface and accelerating the catalytic reaction.

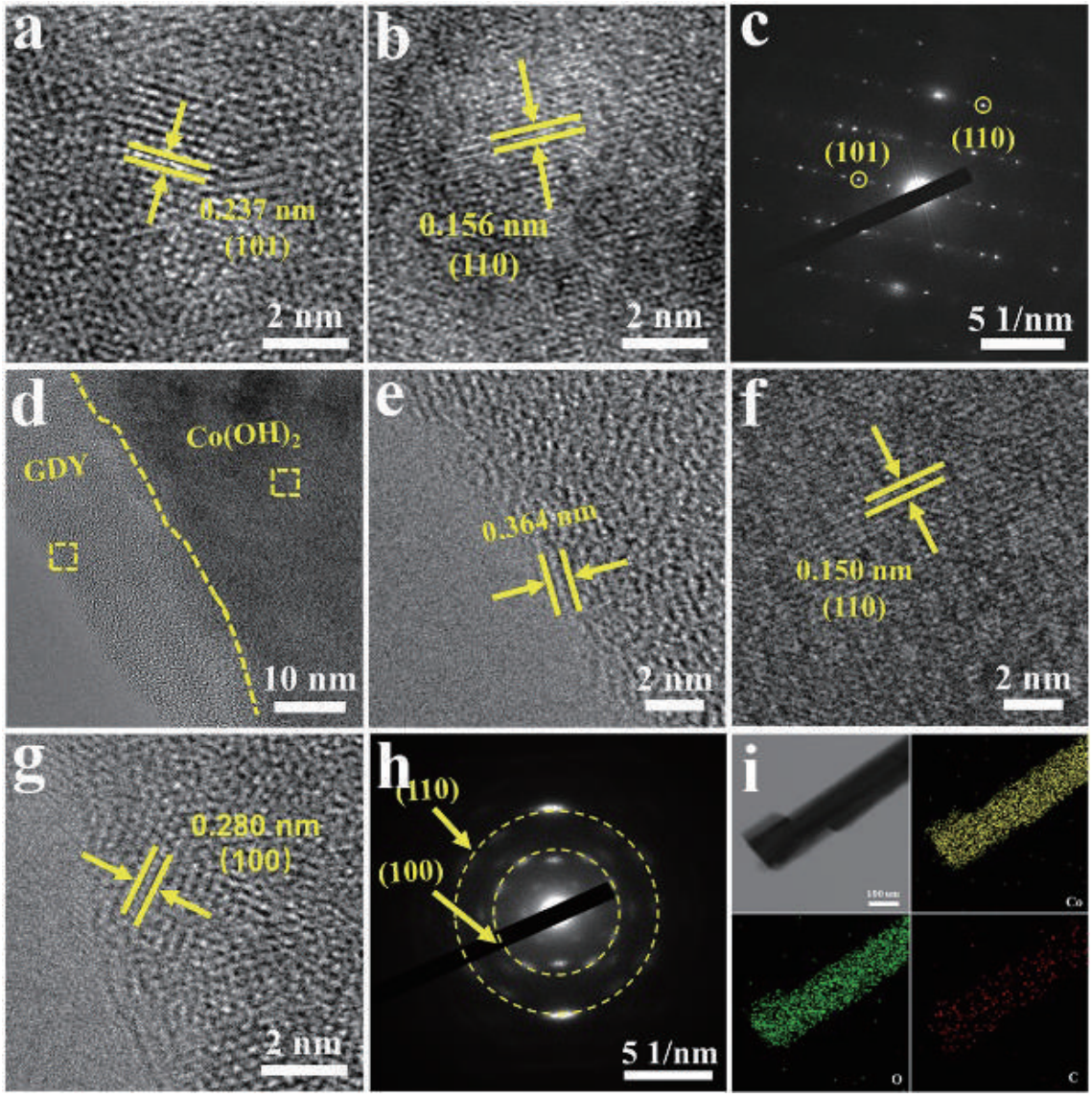

Fig. 3　(a, b) HRTEM images of $Co(OH)_2$. (c) SAED images of $Co(OH)_2$. (d) Interface structure of GDY and $Co(OH)_2$ in GDY/$Co(OH)_2$. (e, f) Enlarged images in the yellow square of (d). (g) HRTEM images of $Co(OH)_2$ phase in GDY/$Co(OH)_2$. (h) SAED pattern of GDY/$Co(OH)_2$. (i) Elemental distribution images of GDY/$Co(OH)_2$

X-ray photoelectron spectroscopy (XPS) results show the copresence of C, Co and O in GDY/$Co(OH)_2$ (Fig. S2), which is consistent with the elemental distribution results (Fig. 2g-i, 3i). The C 1s XPS spectra of GDY/$Co(OH)_2$ show 5 sub-peaks corresponding to sp^2—C (284.52 eV), sp—C (285.26 eV), C—O (286.71 eV), C=O (288.49 eV), and π-π* transition (289.87 eV), respectively (Fig. 4d). The peak area ratio of sp^2—C to sp—C was 1∶2, confirming the successful growth of graphdiyne. Compared with the pristine GDY, the C 1s peak of GDY/$Co(OH)_2$ shifted to higher binding energy by 0.15 eV, and the peak positions of the Co 2p XPS peaks shifted to lower binding energy (Fig. 4e), indicating charge transfer from GDY to $Co(OH)_2$ and further confirming the formation of GDY/$Co(OH)_2$ heterojunction. The emergence of the π-π* transition peaks also confirmed the interaction between GDY and $Co(OH)_2$. As shown in Fig. 4e, the peaks at 797.1 and 781.5 eV corresponded to Co $2p_{1/2}$ and Co $2p_{3/2}$, respectively. The difference in binding energy between these 2 peaks is about 15.6 eV, consistent with the results in the literature[52]. In the Co $2p_{3/2}$ spectrum, the peaks at 781.5 and 786.9 eV corres-

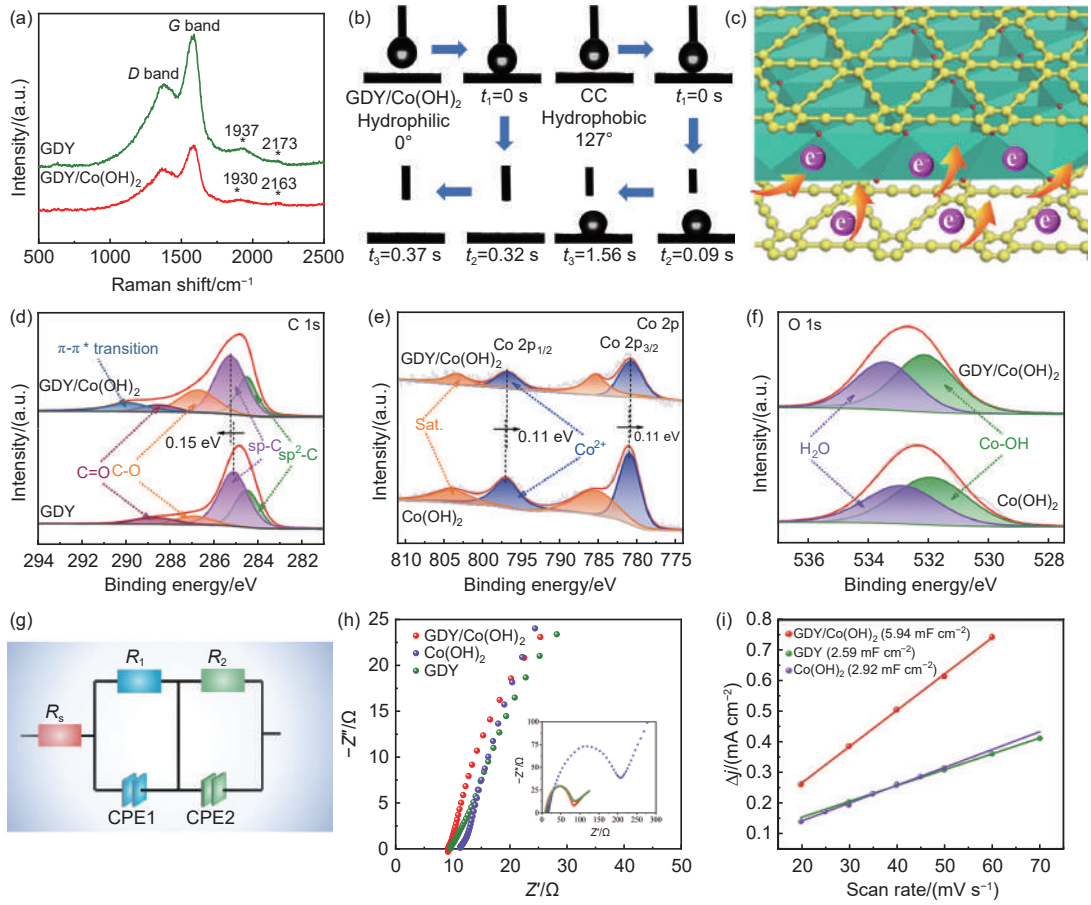

Fig. 4 (a) Raman spectra of GDY and GDY/$Co(OH)_2$. (b) The contact angle test for GDY/$Co(OH)_2$ and CC. (c) Schematic of charge transfer between GDY and $Co(OH)_2$. (d) High-resolution C 1s XPS spectra of GDY and GDY/$Co(OH)_2$. (e) High-resolution Co 2p XPS spectra of $Co(OH)_2$ and GDY/$Co(OH)_2$. (f) High-resolution O 1s XPS spectra of $Co(OH)_2$ and GDY/$Co(OH)_2$. (g) Equivalent circuit model. (h) Electrochemical impedance spectra and (i) Double-layer capacitance test for GDY, $Co(OH)_2$ and GDY/$Co(OH)_2$

pond to the Co^{2+} peak and satellite peaks, respectively. The valence state of Co atoms in GDY/$Co(OH)_2$ remained unchanged compared to $Co(OH)_2$. The O 1s XPS spectra of GDY/$Co(OH)_2$ (Fig. 4f) could be divided into 2 characteristic peaks of Co-OH (532.1 eV) and H_2O (533.4 eV), suggesting that the structural composition of $Co(OH)_2$ did not change after the growth of graphdiyne.

Electrochemical impedance spectra (EIS) and electrochemical active surface area (ECSA) were next studied to determine the origin of the catalytic activity. The Nyquist plots were fitted with the *R*(QR)(QR) circuit model (Fig. 4g) to obtain the charge transfer resistance (R_{ct}) and solution resistance (R_s) (Table S1). The R_{ct} and R_s represent the conductivity and the rate of the electrochemical reaction and mass transfer, respectively. The fitting results showed that GDY/$Co(OH)_2$ had smaller charge transfer resistance and solution resistance (R_{ct} = 79.85 Ω, R_s = 9.48 Ω) compared with pristine $Co(OH)_2$ and GDY (Fig. 4h), indicating higher charge transfer ability, better conductivity, and faster mass transfer. Double layer capacitance values (C_{dl}) were determined by analyzing cyclic voltammetry (CV) curves during non-Faraday intervals at various sweep rates (Fig. S3). The GDY/$Co(OH)_2$ had the highest C_{dl} value (5.94 mF cm^{-2}) among the control samples (Fig. 4i). This indicates that it has the largest electrochemically active surface area and would provide more catalytic active sites. The conductivity of the catalyst has been improved significantly after the in-situ growth of GDY on the $Co(OH)_2$ surface to form a heterostructure. Moreover, the electrochemically active specific surface area of the catalyst was increased, providing a greater abund-

ance of active sites.

The chlorine evolution reaction (CER) performance of the samples were tested using a standard three-electrode system (Fig. 5a). Fig. 5b shows that GDY/$Co(OH)_2$ has the best CER activity with the largest current densities than $Co(OH)_2$ and GDY during the electrocatalysis process. Whereas GDY/$Co(OH)_2$ exhibits a smaller current density in a Cl-free electrolyte than that in Cl-containing electrolyte, which suggests that the primary reaction occurring at the anode is the CER rather than the competitive water splitting reaction. GDY/$Co(OH)_2$ also exhibited a small overpotential of only 83 mV at 10 mA cm^{-2}, better than most of the reported electrocatalysts and control samples of GDY (141 mV) and $Co(OH)_2$ (133 mV) (Fig. 5c and Table S2). Experimental test results also revealed that GDY/$Co(OH)_2$ had the smaller Tafel slope of 30.08 mV dec^{-1} compared with pristine $Co(OH)_2$ and pure GDY (Fig. 5d), indicating the fastest reaction kinetics. The Faradaic efficiency (FE) and active chlorine（AC）yield are examined using DPD spectrophotometry. The chronoamperometry curves and the corresponding UV-vis absorption spectra of the electrolyte for GDY/$Co(OH)_2$ and its control samples were shown in Fig. S4 and Fig. S5, respectively. As shown in Fig. 5f, the Faradaic efficiency of GDY/$Co(OH)_2$ for CER initially increased to a maximum value of 91.54% at 1.8 V (vs. RHE), followed by a slight decrease with the further increase of applied potentials, which might be due to the influence of OER. This value is higher than that of GDY (63.78%) and $Co(OH)_2$ (85.46%). GDY/$Co(OH)_2$ also presents the maximized chlorine yielding rate of 157.11 mg h^{-1} cm^{-2} at 2.1 V (vs. RHE), higher than GDY (46.74 mg h^{-1} cm^{-2}) and $Co(OH)_2$ (136.59 mg h^{-1} cm^{-2}) (Fig. 5g). The comparison of

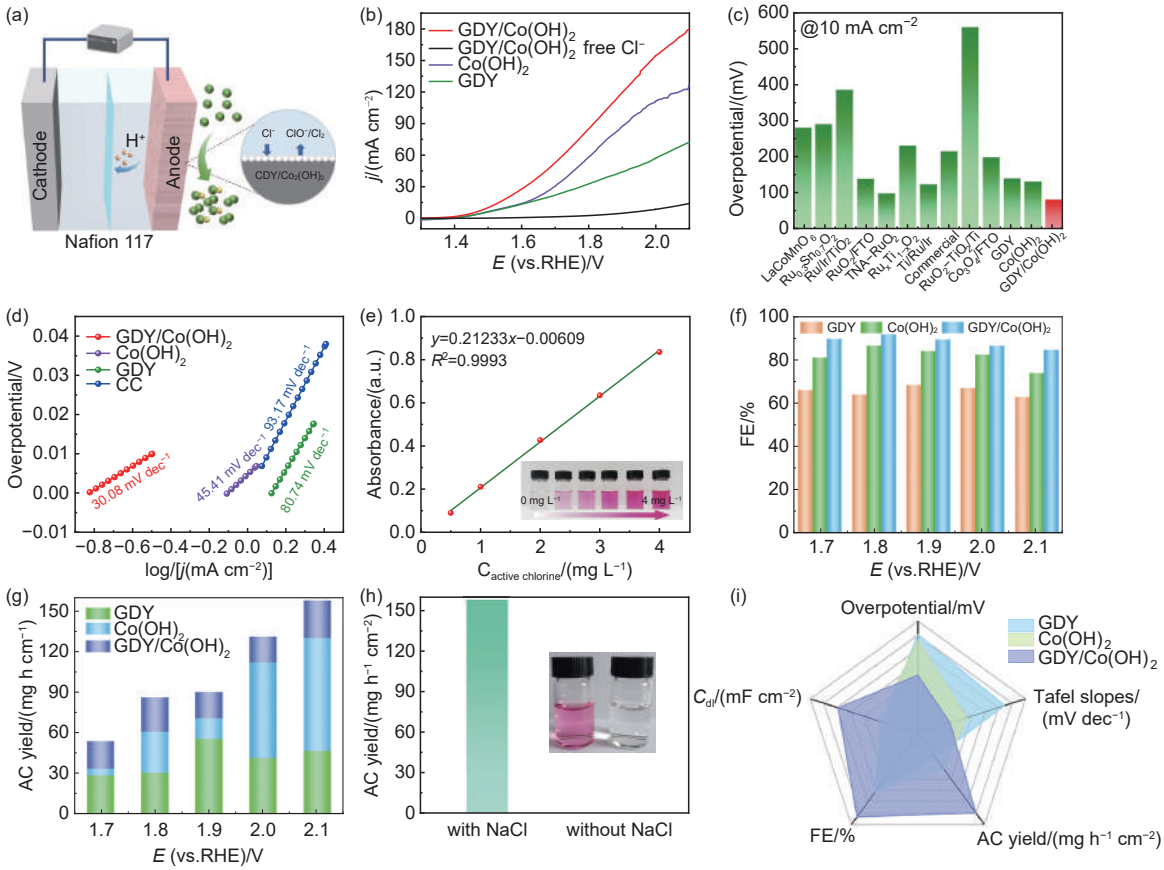

Fig. 5　(a) Schematic of the electrolysis process. (b) LSV curves. (c) Overpotentials at a current density of 10 mA cm^{-2}. (d) Tafel slopes for GDY/$Co(OH)_2$ and its control samples. (e) Determination of standard curves for the detection of active chlorine. Comparison of (f) Faradaic efficiency of active chlorine at various potentials and (g) active chlorine yield at various potentials for GDY, $Co(OH)_2$ and GDY/$Co(OH)_2$. (h) Comparison of active chlorine yield at 2.1 V vs. RHE for GDY/$Co(OH)_2$ with and without NaCl. (i) Comparison of catalytic performance

active chlorine yield at 2.1 V (vs. RHE) in electrolytes with and without NaCl is shown in Fig. 5h, further confirming the primary reaction occurring at the anode is the CER. The GDY/$Co(OH)_2$ heterostructure catalysts exhibited superior activity and selectivity compared to the single-phase catalysts for producing chlorine from electrolytic simulated seawater (Fig. 5i). The stability of the catalyst was tested at 1.5 V (vs. RHE) using the chronoamperometry method (Fig. S6). Fig. 6a shows the LSV curves before and after 10 h of continuous electrolysis. The current density decreased by only 3.51%, demonstrating excellent stability. The XPS tests of the GDY/$Co(OH)_2$ were also conducted after 10 h of electrolysis. As shown in Fig. 6b, the peak area ratio of sp—C to sp^2—C is still 2 : 1, suggesting that the structure of GDY remains intact during electrolysis. The valence state of cobalt remained at +2 after electrolysis, and the structural composition of the catalysts showed no obvious change (Fig. 6c, d). The protective effect of the formed GDY layer is remarkable endowing the catalyst with excellent stability. It is worth noting that there was an evident charge transfer at the heterogeneous interface during the electrolysis process. This transfer could effectively enhance the conductivity of the catalysts, improve the charge transfer ability, and facilitate the kinetics of the catalytic reaction.

4 Conclusion

In summary, we report the in-situ growth of GDY/$Co(OH)_2$ heterointerface structures by growing GDY on $Co(OH)_2$ surface. Experimental results have demonstrated that the as-synthesized catalyst exhibits strong charge transfer between GDY and Co atoms, resulting in the electron-rich heterointerface structures with higher conductivity and more active sites. This significantly enhance the chlorine production se-

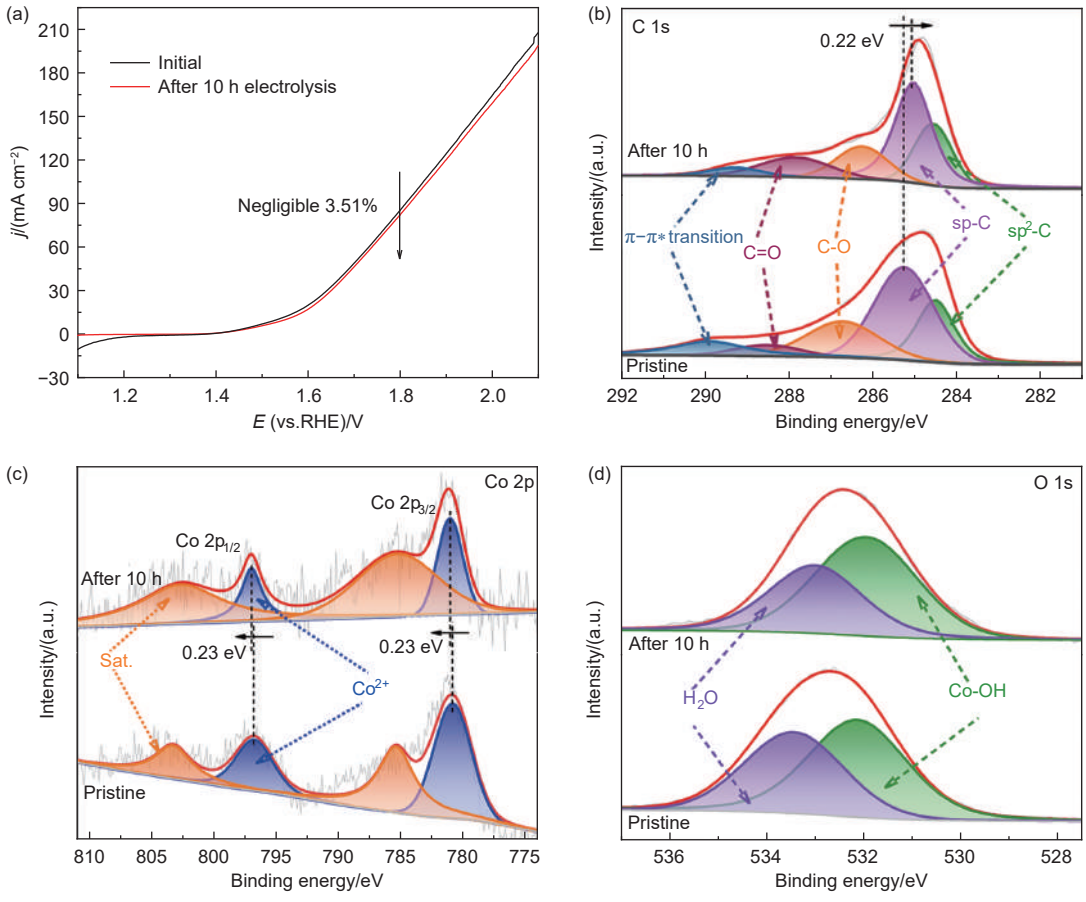

Fig. 6 Comparison of (a) polarization curves, (b) high-resolution C 1s XPS spectra, (c) high-resolution Co 2p XPS spectra and (d) high-resolution O 1s XPS spectra of GDY/$Co(OH)_2$ before and after 10 h of electrolysis of seawater for chlorine production

lectivity (with a high FE of 91.54% at 1.8 V vs. RHE), activity (with a small overpotential of 83 mV at 10 mA cm^{-2}), and stability. This work provides new insights into the design and optimization of efficient catalysts for chlorine production from seawater.

Acknowledgements

This work was supported by the Basic Science Center Project of the National Natural Science Foundation of China (22388101), National Key Research and Development Project of China (2022YFA1204500, 2022YFA1204501, 2022YFA1204503, 2018YFA0703501), the Taishan Scholars Youth Expert Program of Shandong Province (tsqn201909050), and the Natural Science Foundation of Shandong Province (ZR2020ZD38, ZR2021JQ07).

References

[1] Martinez-Huitle C A, Rodrigo M A, Sires I, Scialdone O. A critical review on latest innovations and future challenges of electrochemical technology for the abatement of organics in water[J]. Applied Catalysis B-Environmental, 2023, 328: 122430.

[2] Kleoff M, Vossnacker P, Riedel S. The rise of trichlorides enabling an improved chlorine technology[J]. Angewandte Chemie-International Edition, 2023, 62(17): e202216586.

[3] Vossnacker P, Wüst A, Müller C, et al. Synthesis of a hexachloro sulfate(IV) dianion enabled by polychloride chemistry[J]. Angewandte Chemie-International Edition, 2022, 61(43): e202209684.

[4] Tang C, Zheng Y, Jaroniec M, Qiao S Z. Electrocatalytic refinery for sustainable production of fuels and chemicals[J]. Angewandte Chemie-International Edition, 2021, 60(36): 19572-19590.

[5] Wang Y, Xue Y, Zhang C. Rational surface and interfacial engineering of IrO_2/TiO_2 nanosheet arrays toward high-performance chlorine evolution electrocatalysis and practical environmental remediation[J]. Small, 2021, 17(17): 2006587.

[6] Menzel N, Ortel E, Mette K, et al. Dimensionally stable Ru/Ir/TiO_2-anodes with tailored mesoporosity for efficient electrochemical chlorine evolution[J]. ACS Catalysis, 2013, 3(6): 1324-1333.

[7] He W, Li X, Tang C, et al. Materials design and system innovation for direct and indirect seawater electrolysis[J]. Acs Nano, 2023, 17(22): 22227-22239.

[8] Karlsson R K B, Cornell A. Selectivity between oxygen and chlorine evolution in the chlor-alkali and chlorate processes[J]. Chemical Reviews, 2016, 116(5): 2982-3028.

[9] Yang J, Li W H, Tang H T, et al. CO_2-mediated organocatalytic chlorine evolution under industrial conditions[J]. Nature, 2023, 617(7961): 519-523.

[10] Liu Y, Li C, Tan C, et al. Electrosynthesis of chlorine from seawater-like solution through single-atom catalysts[J]. Nature Communications, 2023, 14(1): 2475-2475.

[11] Zhang X, Wu D, Liu X, et al. Efficient electrocatalytic chlorine evolution under neutral seawater conditions enabled by highly dispersed Co_3O_4 catalysts on porous carbon[J]. Applied Catalysis B: Environmental, 2023, 330: 122594.

[12] Fu X, Zhao X, Lu T B, et al. Graphdiyne-based single-atom catalysts with different coordination environments[J]. Angewandte Chemie-International Edition, 2023, 62(16): e202219242.

[13] Gao X, Liu H, Wang D, Zhang J. Graphdiyne: Synthesis, properties and applications[J]. Chemical Society Reviews, 2019, 48(3): 908-936.

[14] Fang Y, Liu Y, Qi L, et al. 2D graphdiyne: An emerging carbon material[J]. Chemical Society Reviews, 2022, 51(7): 2681-2709.

[15] Zheng X, Chen S, Li J, et al. Two-dimensional carbon graphdiyne: Advances in fundamental and application research[J]. Acs Nano, 2023, 17(15): 14309-14346.

[16] Luan X, Qi L, Zheng Z, et al. Step by step induced growth of zinc-metal interface on graphdiyne for aqueous zinc-ion batteries[J]. Angewandte Chemie-International Edition, 2023, 62(8): e202215968.

[17] Xing C, Xue Y, Zheng X, et al. Highly selective electrocatalytic olefin hydrogenation in aqueous solution[J]. Angewandte Chemie-International Edition, 2023, 62(41): e202310722.

[18] Zheng Z, Qi L, Gao Y, et al. Ir-0/graphdiyne atomic interface for selective epoxidation[J]. National Science Review, 2023, 10(8): nwad156.

[19] Li G, Li Y, Liu H, et al. Architecture of graphdiyne nanoscale films[J]. Chemical Communications, 2010, 46(19): 3256-3258.

[20] Zhang D, Xue Y, Zheng X, et al. Multi-heterointerfaces for selective and efficient urea production[J]. National Science Review, 2023, 10(2): nwac209.

[21] Qi L, Gao Y, Gao Y, et al. Controlled growth of metal atom arrays on graphdiyne for seawater oxidation[J]. Journal of the American Chemical Society, 2024, 146(8): 5669-5677.

[22] Liu Y, Gao Y, He F, et al. Controlled growth interface of charge transfer salts of nickel-7, 7, 8, 8-tetracyanoquinodimethane on surface of graphdiyne[J]. CCS Chemistry, 2023, 5(4): 971-981.

[23] Zheng X, Xue Y, Zhang C, Li Y. Controlled growth of multidimensional interface for high-selectivity ammonia production[J]. CCS Chemistry, 2023, 5(7): 1653-1662.

[24] Yang Q, Guo Y, Yan B, et al. Hydrogen-substituted graphdiyne ion tunnels directing concentration redistribution for commercial-grade dendrite-free zinc anodes[J]. Advanced Materials, 2020, 32(25): 2001755.

[25] Yang Q, Li L, Hussain T, et al. Stabilizing interface pH by N-modified graphdiyne for dendrite-free and high-rate aqueous Zn-ion batteries[J]. Angewandte Chemie-International Edition, 2022, 61(6): e202112304.

[26] Zhang S, Kong Y, Gu Y, et al. Strong d-π orbital coupling of Co-C_4

atomic sites on graphdiyne boosts potassium-sulfur battery electrocatalysis[J]. Journal of the American Chemical Society, 2024, 146(7): 4433-4443.

[27] Zheng X, Wu H, Gao Y, et al. Controllable assembly of highly oxidized cobalt on graphdiyne surface for efficient conversion of nitrogen into nitric acid[J]. Angewandte Chemie-International Edition, 2024, 63(9): e2023167.

[28] Shi G, Xie Y, Du L, et al. Stabilization of cobalt clusters with graphdiyne enabling efficient overall water splitting[J]. Nano Energy, 2020, 74: 104852.

[29] Gao Y, Qi L, He F, et al. Selectively growing a highly active interface of mixed Nb-Rh oxide/2D carbon for electrocatalytic hydrogen production[J]. Advanced Science, 2022, 9(10): 2104706.

[30] Gao Y, Xue Y, Liu T, et al. Bimetallic mixed clusters highly loaded on porous 2D graphdiyne for hydrogen energy conversion[J]. Advanced Science, 2021, 8(24): 2102777.

[31] Gao Y, Xue Y, Qi L, et al. Rhodium nanocrystals on porous graphdiyne for electrocatalytic hydrogen evolution from saline water[J]. Nature Communications, 2022, 13(1): 5227.

[32] Gao Y, Xue Y, Wu H, et al. Self-organized gradually single-atom-layer of metal osmium for an unprecedented hydrogen production from seawater [J]. Journal of the American Chemical Society, 2024:https://doi.org/10.1021/jacs.1024c00027.

[33] Yang Q, Guo Y, Gu J, et al. Scalable synthesis of 2D hydrogen-substituted graphdiyne on Zn substrate for high-yield N_2 fixation[J]. Nano Energy, 2020, 78: 105283.

[34] Guo Y, Liu J, Yang Q, et al. Regulating nitrogenous adsorption and desorption on Pd clusters by the acetylene linkages of hydrogen substituted graphdiyne for efficient electrocatalytic ammonia synthesis[J]. Nano Energy, 2021, 86: 106099.

[35] Guo Y, Liu J, Yang Q, et al. Metal-tuned acetylene linkages in hydrogen substituted graphdiyne boosting the electrochemical oxygen reduction[J]. Small, 2020, 16(10): 1907341.

[36] Guo Y, Zhang R, Zhang S, et al. Steering sp-carbon content in graphdiynes for enhanced two-electron oxygen reduction to hydrogen peroxide [J]. Angewandte Chemie-International Edition, 2024: e202401501.

[37] Shi G, Xie Y, Du L, et al. Constructing Cu-C bonds in a graphdiyne-regulated Cu single-atom electrocatalyst for CO_2 reduction to CH_4[J]. Angewandte Chemie-International Edition, 2022, 61(23): e202203569.

[38] Feng X, Liu J, Chen L, et al. Hydrogen radical-induced electrocatalytic N_2 reduction at a low potential[J]. Journal of the American Chemical Society, 2023, 145(18): 10259-10267.

[39] Hui L, Xue Y, Xing C, et al. Atomic alloys of nickel-platinum on carbon network for methanol oxidation[J]. Nano Energy, 2022, 95: 106984.

[40] Hui L, Zhang X, Xue Y, et al. Highly dispersed platinum chlorine atoms anchored on gold quantum dots for a highly efficient electrocatalyst[J]. Journal of the American Chemical Society, 2022, 144(4): 1921-1928.

[41] Zhang X, Hui L, Yan D, et al. Defect rich structure activated 3D palladium catalyst for methanol oxidation reaction[J]. Angewandte Chemie-International Edition, 2023, 62(40): e202308968.

[42] Zhong M X, Xu M J, Ren S Y, et al. Modulating the electronic structure of $Ni(OH)_2$ by coupling with low-content Pt for boosting the urea oxidation reaction enables significantly promoted energy-saving hydrogen production[J]. Energy & Environmental Science, 2024, 17(5): 1984-1996.

[43] Song N, Ren S Y, Zhang Y, et al. Confinement of prussian blue analogs boxes inside conducting polymer nanotubes enables significantly enhanced catalytic performance for water treatment[J]. Advanced Functional Materials, 2022, 32(34): 2204751.

[44] Lin X, Zhang S-N, Xu D, et al. Electrochemical activation of C-H by electron-deficient W_2C nanocrystals for simultaneous alkoxylation and hydrogen evolution[J]. Nature Communications, 2021, 12(1): 3882.

[45] Xu D, Lin X, Li Q Y, et al. Boosting mass exchange between Pd/NC and MoC/NC dual junctions via electron exchange for cascade CO_2 fixation[J]. Journal of the American Chemical Society, 2022, 144(12): 5418-5423.

[46] Lin X, Zhou Z Y, Li Q Y, et al. Direct oxygen transfer from H_2O to cyclooctene over electron-rich RuO_2 nanocrystals for epoxidation and hydrogen evolution[J]. Angewandte Chemie-International Edition, 2022, 61(35): e202207108.

[47] Wang N, Song S Z, Wu W T, et al. Bridging laboratory electrocatalysts with industrially relevant alkaline water electrolyzers [J]. Advanced Energy Materials, 2024: 2303451.

[48] Tang C, Chen L, Li H, et al. Tailoring acidic oxygen reduction selectivity on single-atom catalysts via modification of first and second coordination spheres[J]. Journal of the American Chemical Society, 2021, 143(20): 7819-7827.

[49] Tang C, Jiao Y, Shi B, et al. Coordination tunes selectivity: two-electron oxygen reduction on high-loading molybdenum single-atom catalysts[J]. Angewandte Chemie-International Edition, 2020, 59(23): 9171-9176.

[50] Zhu X, Wang P, Wang Z, et al. Co_3O_4 nanobelt arrays assembled with ultrathin nanosheets as highly efficient and stable electrocatalysts for the chlorine evolution reaction[J]. Journal of Materials Chemistry A, 2018, 6(26): 12718-12723.

[51] Xiao M, Wu Q, Ku R, et al. Self-adaptive amorphous CoO_xCl_y electrocatalyst for sustainable chlorine evolution in acidic brine[J]. Nature Communications, 2023, 14(1): 5356.

[52] Qi D, Xu J, Zhou Y, et al. Cyclodextrin-supported $Co(OH)_2$ clusters as electrocatalysts for efficient and selective H_2O_2 synthesis[J]. Angewandte Chemie-International Edition, 2023, 62(37): e202307355.